The interaction of carbon nanotubes (CNTs) with CuCoO$_2$ nanosheets promotes the structural modification and enhances their OER performance

Shiyu Ma,[†,a] Chao Jiang,[†,a] Jilin Bai,*[,a] Li Sun,[a] Hao Tan,[a,b] Lifeng Liu,[b] Xianwei Zeng,[c] Xiujian Zhao,[a] and Dehua Xiong*[,a]

a.State Key Laboratory of Silicate Materials for Architectures, Wuhan University of Technology, Wuhan 430070, P. R. China.

*Corresponding author email: baijilin520@whut.edu.cn (J. Bai), xiongdehua2010@gmail.com (D. Xiong).

b.Songshan Lake Materials Laboratory, Dongguan, 523808, P. R. China.

c.Zhejiang Kelei New Material Co., Ltd., Huzhou, 313300, P. R. China

† Shiyu M. and Chao J. contributed equally in this work.

List of contents:

Experimental details

Materials synthesis

All chemicals in the experiment were of analytical grade without further purification. Cu-BTC and $CuCoO_2$ were prepared according to our previous work.

Cu-BTC synthesis: Firstly, 2.6093 g $Cu(NO_3)_2 \cdot 3H_2O$, 1.2600 g H_3BTC and 9 mL isopropyl alcohol (IPA) were dissolved in 27 mL deionized (DI) water and 36 mL absolute ethanol (ET), and magnetically stirring for 30 minutes. Secondly, the solution was transferred into a 100 mL Teflon lined autoclave and kept at 120 °C for hydrothermal reaction for 12 h. Afterwards, the resulting blue precipitate was washed three times with ET to remove any by-product impurities. Finally, the Cu-BTC was dried at 70 °C for 5 h for further use.

CNT-supported $CuCoO_2$ synthesis: Firstly, 1.50 g Cu-BTC, 1.60 g (5.5 mmol) $Co(NO_3)2 \cdot 6H_2O$, CNTs of different quality (0.2204 g, 0.4408 g and 0.6612 g) and 1.40g NaOH were dissolved in DI water and ET, and magnetically stirring for 30 minutes. Secondly, the 30 mmol PVP (K23-27) was added to the above solution and stirred for 1 h. Afterwards, the solution was transferred into a 100 mL Teflon lined autoclave and kept at 140 °C for hydrothermal reaction for 24 h. Finally, the obtained precipitate was washed several times with ammonia, DI water, and ET, and then dried at 70 °C for 5 h for further characterization. For comparison, we also prepared $CuCoO_2$ without CNTs, which was prepared in the same way as above, except that CNTs was not added.

Structural characterization

The crystal phase of samples was characterized by the X-ray diffraction (XRD, D8 Advance, Bruker, Germany). The lattice parameters were obtained by Rietveld refinement using the General Structure Analysis System (GSAS).[1-3] The morphology, microstructure, and chemical composition of the samples were examined by field-emission scanning electron microscopy (FESEM, Sigma 300, Zeiss, Germany) and transmission electron microscopy (TEM, JEM-2100 operating at 200 keV, JEOL, Japan) equipped with energy-dispersive X-ray spectroscopy (EDS). The element proportion of the samples was analyzed by inductively coupled plasma-atomic emission spectrometry (ICP-AES, Prodigy 7, LEEMAN LABS, USA). The surface chemical states of the samples were analyzed by X-ray photoelectron spectroscopy (XPS, Escalab 250Xi, Thermo Fisher Scientific, USA). The C 1s line (284.80 eV) corresponding to the surface adventitious carbon (C-Cline bond) has been used as the reference binding energy. The structure of samples was investigated by Raman (LabRAM Odyssey, HORIBA Scientific, France) and in situ Raman (LabRam HR Evolution, HORIBA Scientific, France). The Brunauer-Emmett-Teller (BET) specific surface areas and porosity parameters of the samples were taken by N_2 adsorption-desorption isothermetry (TriStar II 3020, Micromeritics, USA). The oxygen vacancy defect of catalyst was detected by electron paramagnanetic resonance (EPR, A300-10/12, Bruker, Germany). The absorption curve of catalyst in 200-2500 nm range

was measured by UV-visible near-infrared spectrophotometer (UV-vis, Lambda 750 S, PerkinElmer, USA), and the band gap width was calculated. Thermogravimetric Analysis- differential scanning calorimetry (TG-DSC, STA449F3, NETZSCH, Germany) were conducted. TPR and TPD testing by automatic chemisorption instrument (BSD-Chem C200, BSD Instrument, Chian). Zeta potential was measured by laser particle size analyzer (Zetasizer Nano ZS90, Malvern, Britain).

Electrode preparation and electrochemical measurement

Firstly, 15 mg $CuCoO_2$ was dissolved in 500 μL DI water, 480 μL IPA and 20 μL Nafion (5 wt%, Sigma) to make a suspension, then 20 μL of the suspension solution was placed on Ni foam (1 cm×1 cm), and finally the working electrode was prepared by drying at 150 °C for 10 min.

The OER performance was evaluated by cyclic voltammetry (CV) and electrochemical impedance spectroscopy (EIS) in a three-electrode configuration in 1.0 M KOH (pH = 13.5) using a CS2350H electrochemical workstation (Wuhan Corrtest Instruments Corp., China). A platinum wire and a saturated calomel electrode (SCE)were used as the counter and reference electrodes, respectively. Cyclic voltametric (CV) scans were recorded between 1.05 and 1.80 V vs. reversible hydrogen electrode (RHE) at a scan rate of 2 mV·s^{-1}. In addition, two types of CV curves were recorded. On the one hand, CV is measured at different rates (from 20 to 100 mV·s^{-1}) in the non-Faraday potential window (-0.05-0.05 V vs. SCE) to determine the electrochemical double-layer capacitance (C_{dl}) and the electrochemical surface area (ECSA). On the other hand, CV is measured at different rates (5 mV·s^{-1}, 10 mV·s^{-1}, 20 mV·s^{-1}, 30 mV·s^{-1}, 40 mV·s^{-1} and 50 mV·s^{-1}) in the potential window in which the redox reaction occurs (1.05-1.60 V vs. RHE) to analyze the rate constant of metal redox by Laviron equation. The EIS measurements were performed in the frequency range of 100 kHz-10 mHz under a constant potential of 1.63 V vs. RHE. Under the constant current density of 10 mA cm^{-2}, the stability ofthe sample was tested for 18 hours.

All current density values are normalized with respect to the geometrical surface area of the working electrode. All CV curves presented in this work are iR-corrected (85%). The correction was done according to the following equation:

$$E_c = E_m - iR_s \tag{S1}$$

where E_c is the iR-corrected potential, Em experimentally measured potential, and R_s the equivalent series resistance extracted from the electrochemical impedance spectroscopy measurements. Unless otherwise specified, all potentials are reported vs. RHE by converting the potentials measured vs. SCE according to the following formula:

$$E (RHE) = E (SCE) + 0.241 + 0.059 \text{ pH} \tag{S2}$$

ECSA can be calculated by the equation:

$$ECSA = (C_{dl}/C_s) \times A \tag{S3}$$

C_{dl} is the double-layer capacitances value. C_s is the specific capacitance (typically 0.04 mF cm^{-2}). A represents the actual area of the efficient working electrode.

Laviron equation.

$$E_p = E_{1/2} - (RT/\alpha nF) \times [\ln(\alpha nF/RTk_s) + \ln(\upsilon)] \qquad (S4)$$

where E_p is the reduction potential of metal redox, $E_{1/2}$ is the formal potential of metal redox, R is universal gas constant, T is temperature in Kelvin, n is number of electrons transferred, α is the transfer coefficient, k_s is the rate constant of metal redox, and υ is scan rate in the CV measurement.

Theoretical Details

We have employed the first-principles [4, 5] to perform density functional theory (DFT) calculations within the generalized gradient approximation (GGA) using the Perdew-Burke-Ernzerhof (PBE) [6] formulation. We have chosen the projected augmented wave (PAW) potentials [7, 8] to describe the ionic cores and take valence electrons into account using a plane wave basis set with a kinetic energy cutoff of 520 eV. The GGA+U method was adopted in our calculations. The value of the effective Hubbard U was set as 5.125 eV for Co Partial occupancies of the Kohn-Sham orbitals were allowed using the Gaussian smearing method with a width of 0.05 eV. The electronic energy was considered self-consistent when the energy change was smaller than 10^{-5} eV. A geometry optimization was considered convergent when the energy change was smaller than 0.05 eV $Å^{-1}$. The Brillouin zone integration is performed using 2×2×1 Monkhorst-Pack k-point sampling for a structure. Finally, the adsorption energies(Eads) were calculated as Eads= Ead/sub -Ead - Esub, where Ead/sub, Ead, and Esub are the total energies of the optimized adsorbate/substrate system, the adsorbate in the structure, and the clean substrate, respectively. The free energy was calculated using the equation:

G=Eads+ZPE-TS $\qquad\qquad\qquad$ (S5)

where G, Eads, ZPE and TS are the free energy, total energy from DFT calculations, zero point energy and entropic contributions, respectively, where T is set to 300K.

Supplementary table:

Table S1. Detailed reaction conditions for synthesizing delafossite $CuCoO_2$ nanosheets.

Sample	Cu-BTC-IPA (g)	Co(NO$_3$)$_2$ (mmol)	CNTs (g)	NaOH (g)	PVP (mmol)	Solvent (mL)	Temp. (°C)	Time (h)
CCO			0					
CCO/25CNT	1.5	5.5	0.2204	1.40	30	50 ET:20 DI	140	24
CCO/50CNT			0.4408					
CCO/75CNT			0.6612					

Table S2. Results of structure analysis calculated from XRD Rietveld refinement of CCO and CCO/xCNT (x=25, 50, 75).

Sample	O-Cu	O-Co	V (Å)	R_{wp}	R_p
CCO	2.158	1.7780	119.643	1.80%	1.30%
CCO/25CNT	2.006	1.8399	119.557	1.73%	1.39%
CCO/50CNT	1.956	1.8630	119.591	2.17%	1.78%
CCO/75CNT	1.897	1.8901	119.495	1.85%	1.47%

Table S3. The OER performance of these electrodes in this work compared with other oxide catalysts.

Catalyst	Electrolyte	η_{10} (mV)	Tafel slope (mV dec^{-2})	(year)[Ref.]
Ni@RuO$_2$		283	60	This
Ni@CCO/50CNT		343	65	work
Fe-CuCoO$_2$		369	69	(2023)[9]
CuCoO$_2$		378	85	(2023)[10]
CuGaO$_2$		400	61	(2022)[11]
SrLaCoO$_4$	1.0 M KOH	370	78.4	(2023)[12]
Sr$_2$CoFeO$_6$		360	70.81	(2023)[13]
SnCo$_2$O$_4$		343	58.93	(2024)[14]
NiFe$_2$O$_4$		366	84.2	(2023)[15]
Ni$_x$Co$_{1-x}$@Ni$_x$Co$_{1-x}$O/NCNT		380	65	(2023)[16]
CoSnS@CNT		350	75	(2020)[17]

Table S4. BET specific surface area, pore volume and pore diameter of CCO and CCO/xCNT (x=25, 50, 75).

Sample	BET specific surface area (m^2 g^{-1})	BJH desorption cumulative pore volume (cm^3 g^{-1})	BJH desorption average pore diameter (nm)
CCO	10.5507	0.026704	10.8914
CCO/25CNT	18.3712	0.066635	14.8005
CCO/50CNT	27.2150	0.104081	15.4043
CCO/75CNT	31.2282	0.123917	15.4252

Supplementary figures:
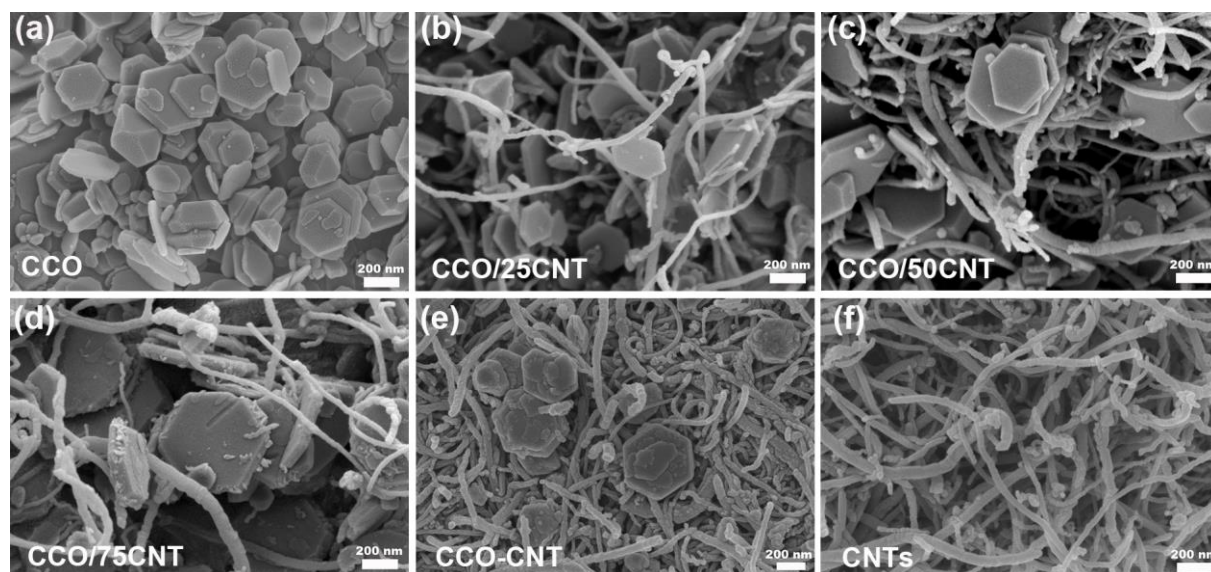
Fig. S1. SEM images of CCO (a), CCO/25CNT (b), CCO/50CNT (c), CCO/75CNT (d), CCO-CNT (e) and CNTs (f).
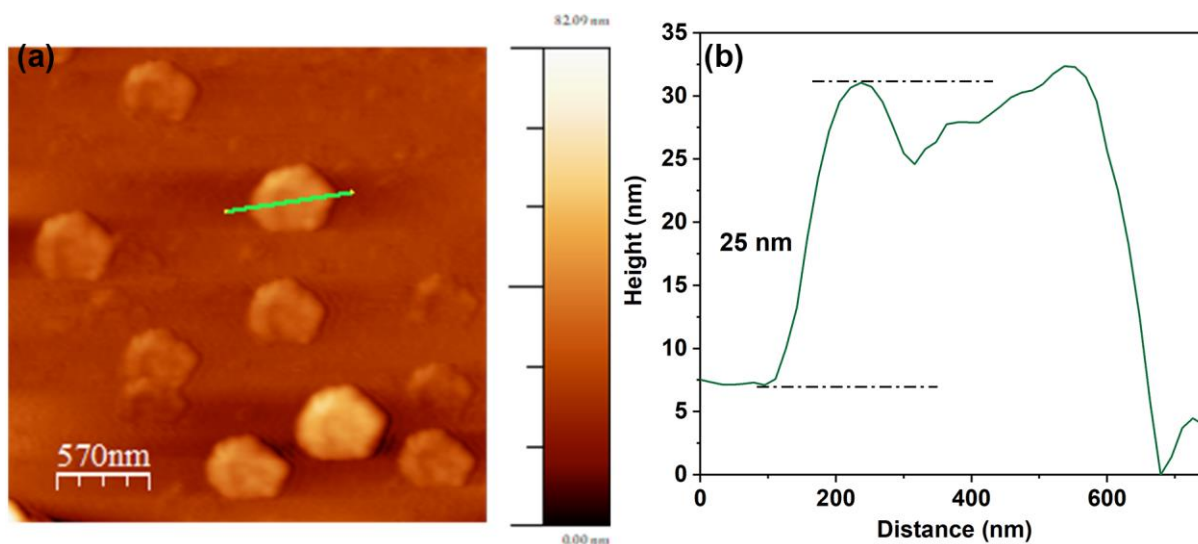
Fig. S2. AFM images (a) and the height profiles (b) of CCO/50CNT.
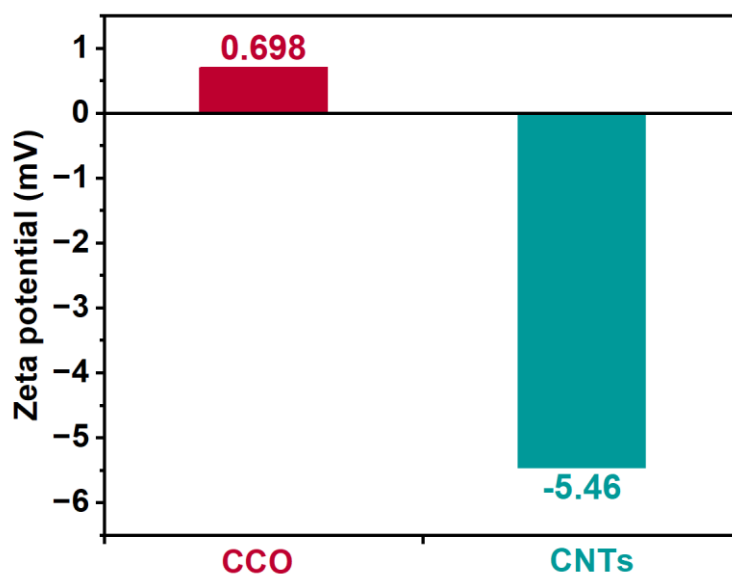
Fig. S3. Zeta potential of CCO and CNTs.
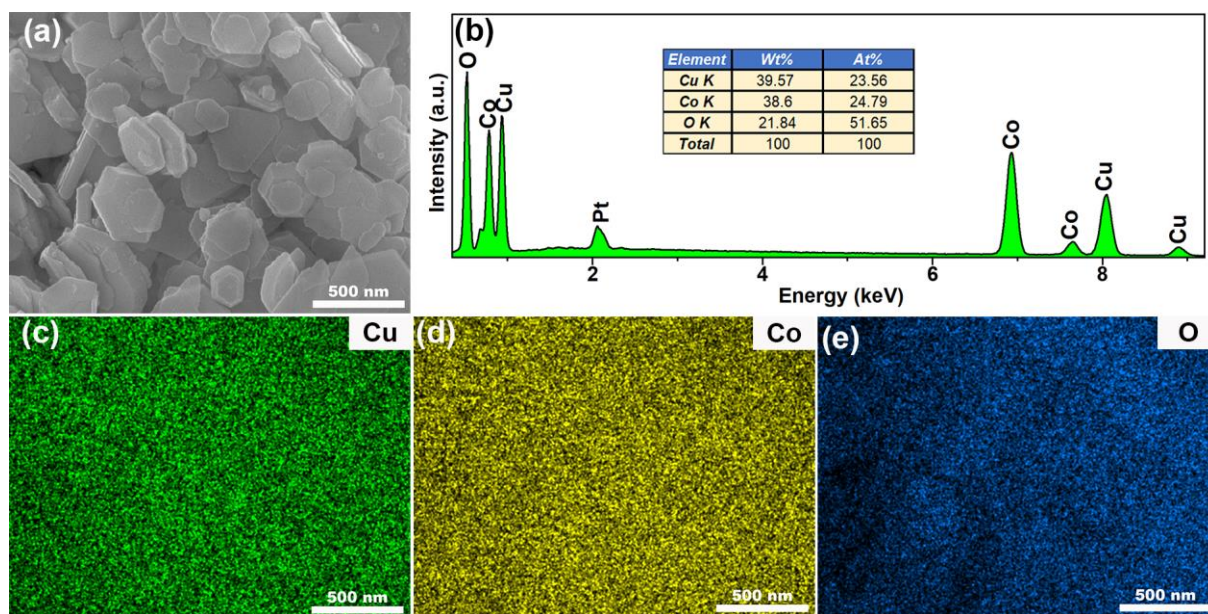
Fig. S4. SEM image (a), EDS spectrum (b) and elemental maps (c-e) of CCO.
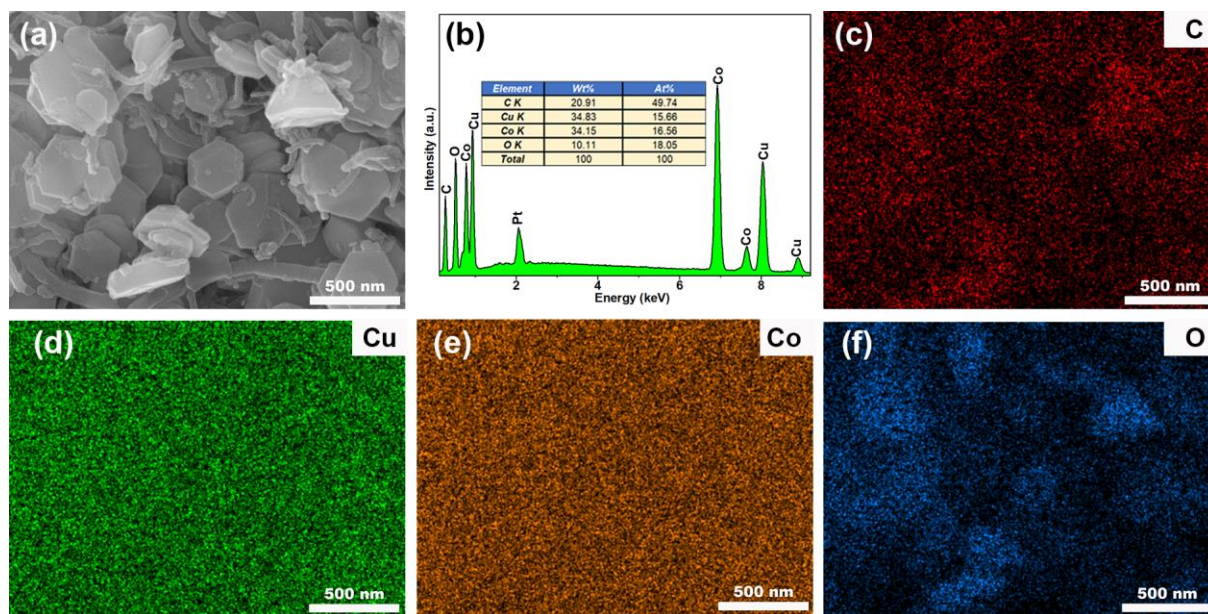
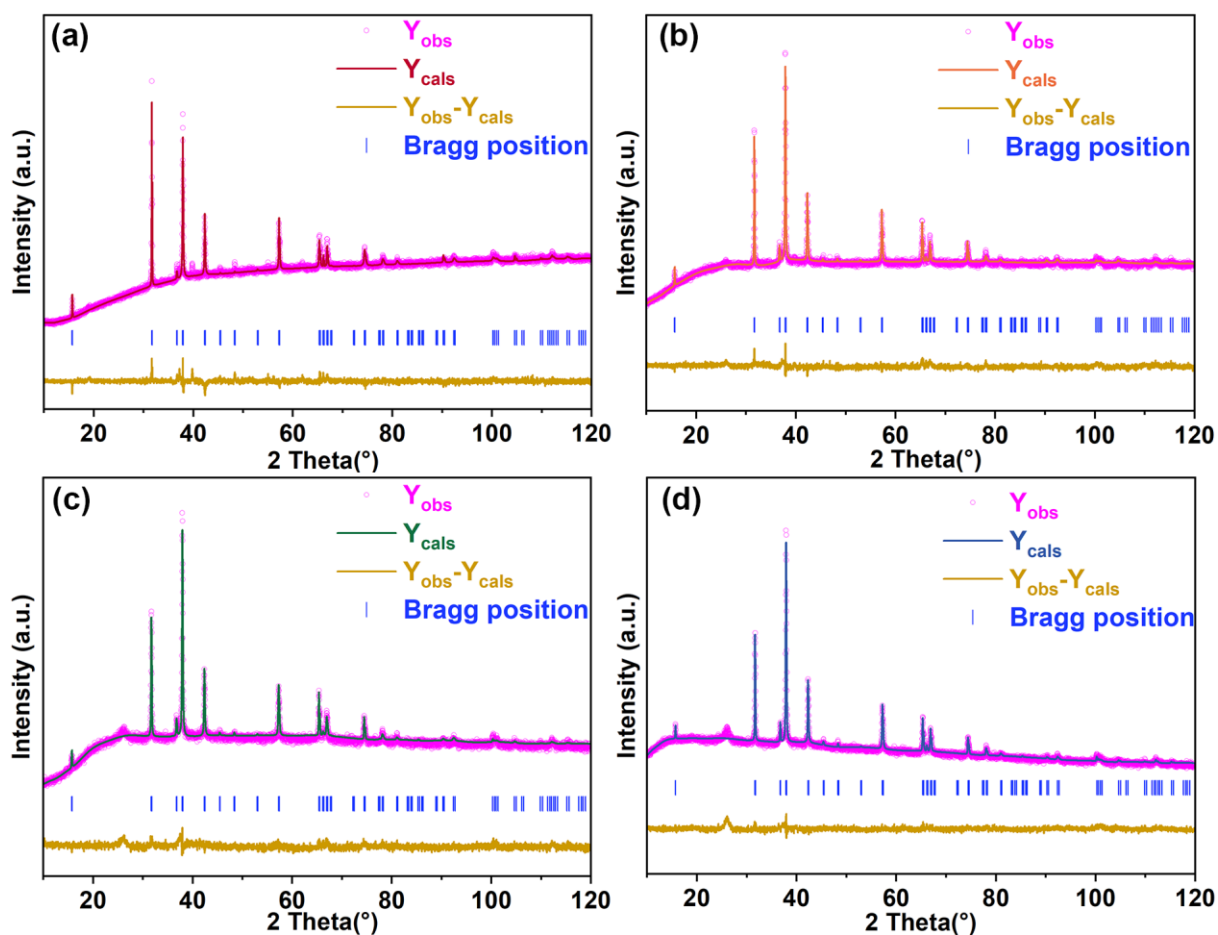**Fig. S5.** SEM image (a), EDS spectrum (b) and elemental maps (c-f) of CCO/25CNT.
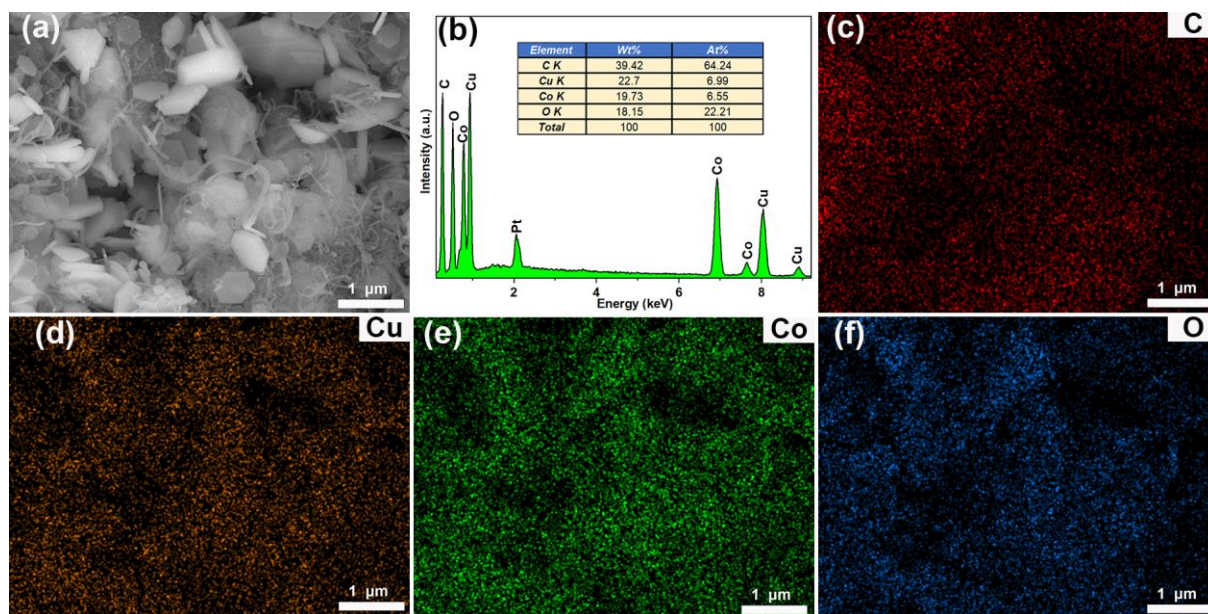
Fig. S6. SEM image (a), EDS spectrum (b) and elemental maps (c-f) of CCO/50CNT.
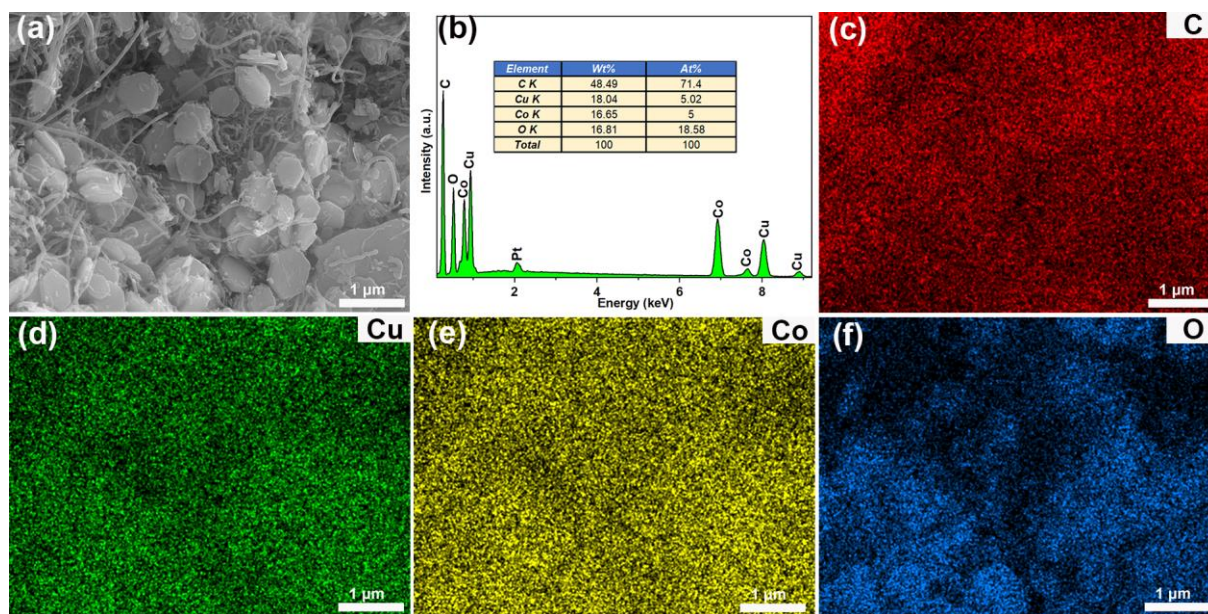
Fig. S7. SEM image (a), EDS spectrum (b) and elemental maps (c-f) of CCO/75CNT.

Fig. S8. Rietveld refined XRD pattern (a, CCO; b, CCO/25CNT; c, CCO/50CNT; d, CCO/75CNT) of the CCO and CCO/xCNT (x=25, 50, 75).
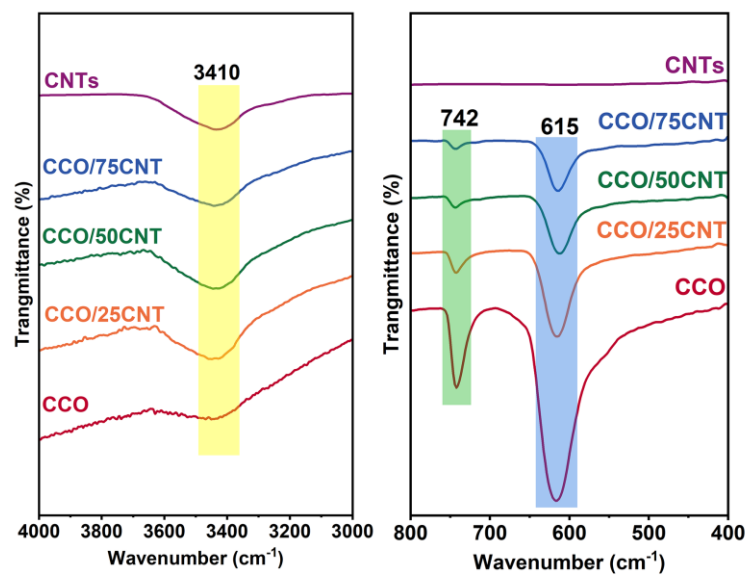
Fig. S9. Fourier transform infrared spectra of CNTs, CCO and CCO/xCNT (x=25, 50 and 75).
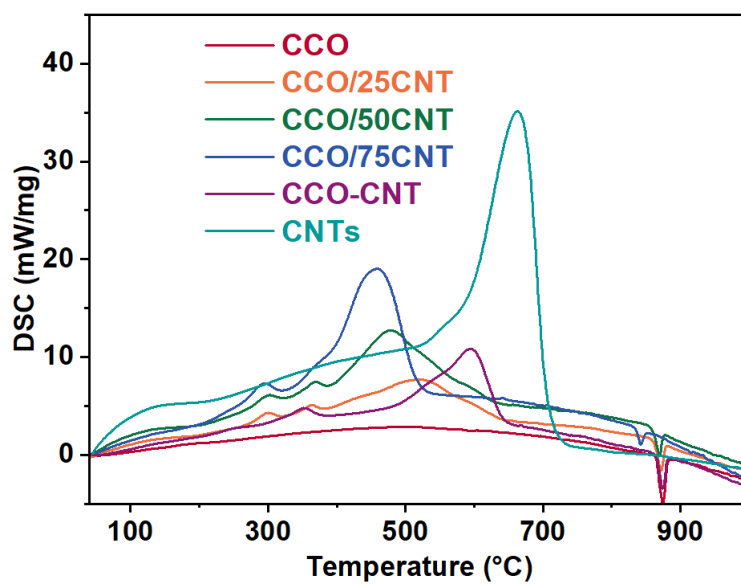
Fig. S10. DSC curves of CCO, CCO/xCNT (x=25, 50 and 75), CCO-CNT and CNTs.
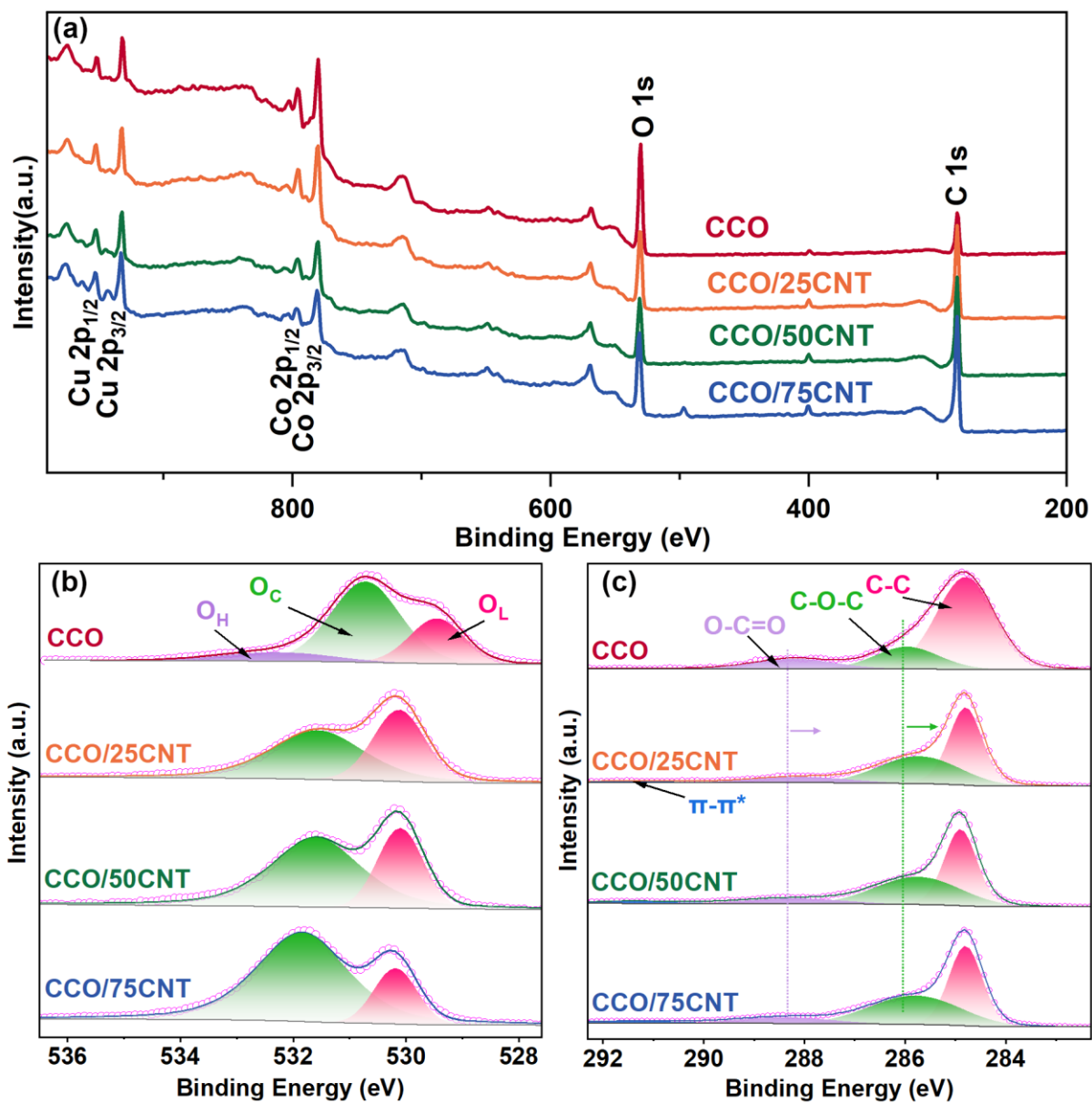
Fig. S11. The XPS survey spectra (a), O 1s (b) and C 1s (c) high-resolution XPS spectra of CCO and CCO/xCNT (x=25, 50 and 75).
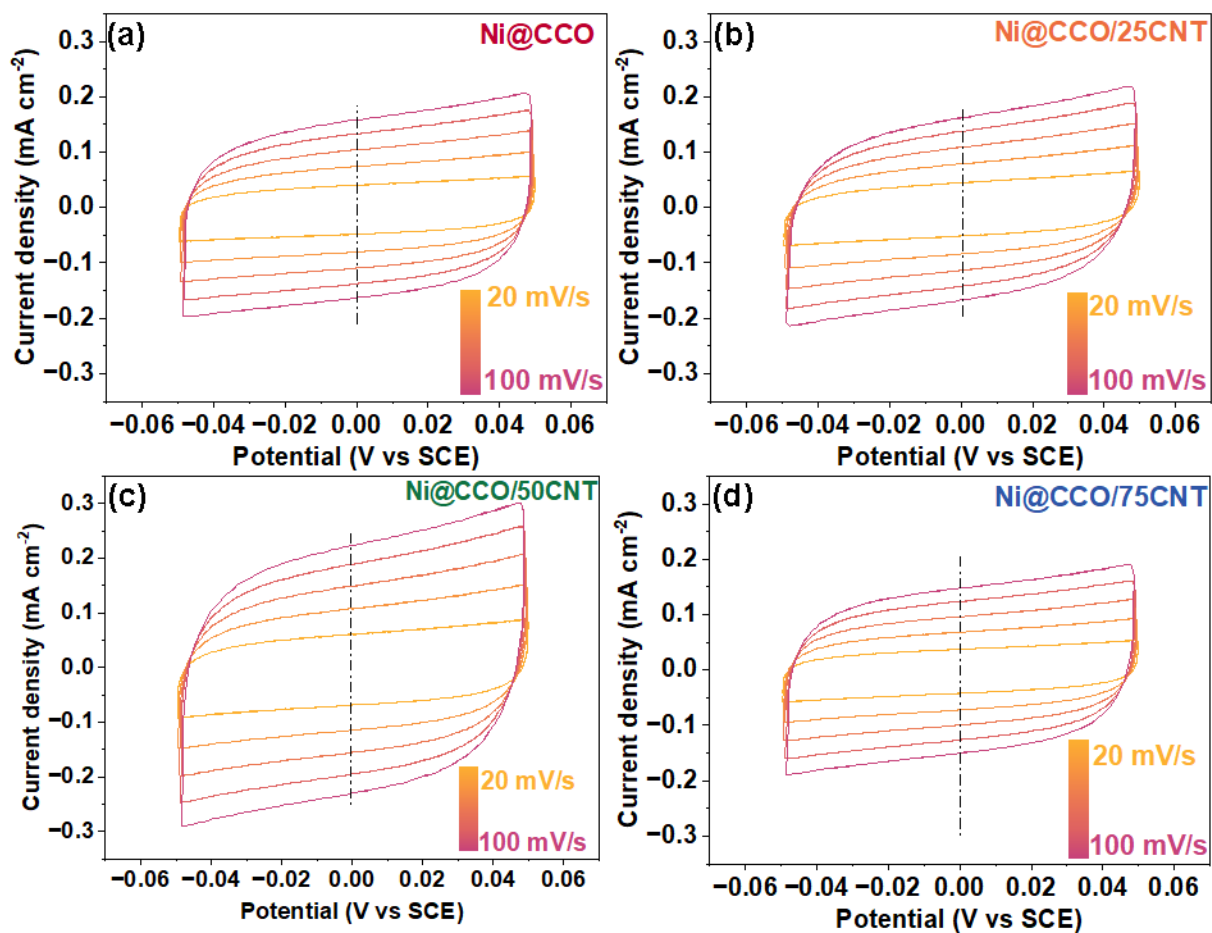
Fig. S12. CV curves of Ni@CCO (a), Ni@CCO/25CNT (b), Ni@CCO/50CNT (c) and Ni@CCO/75CNT (d) at different sweep speeds (such as 20, 40, 60, 80, 100 mV/s).
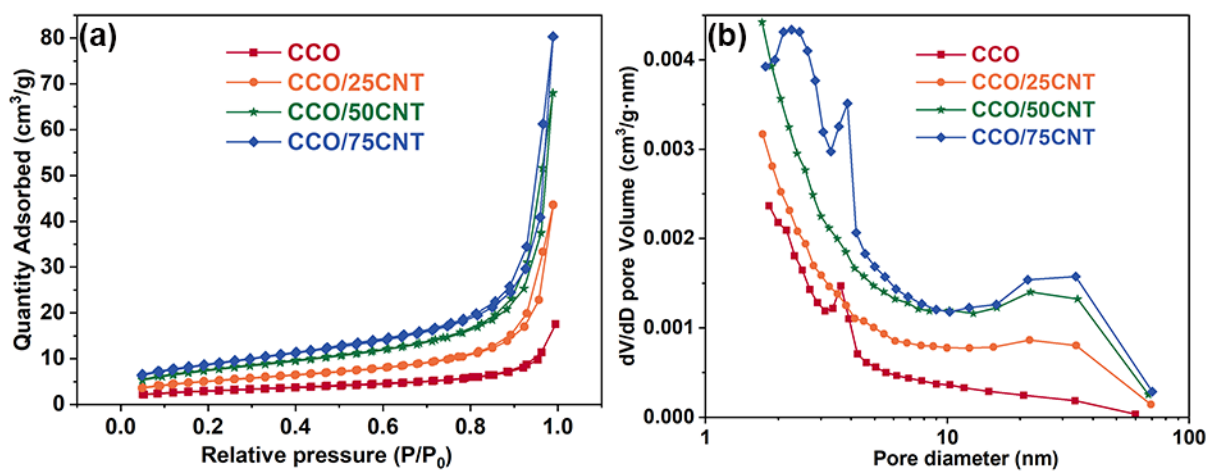

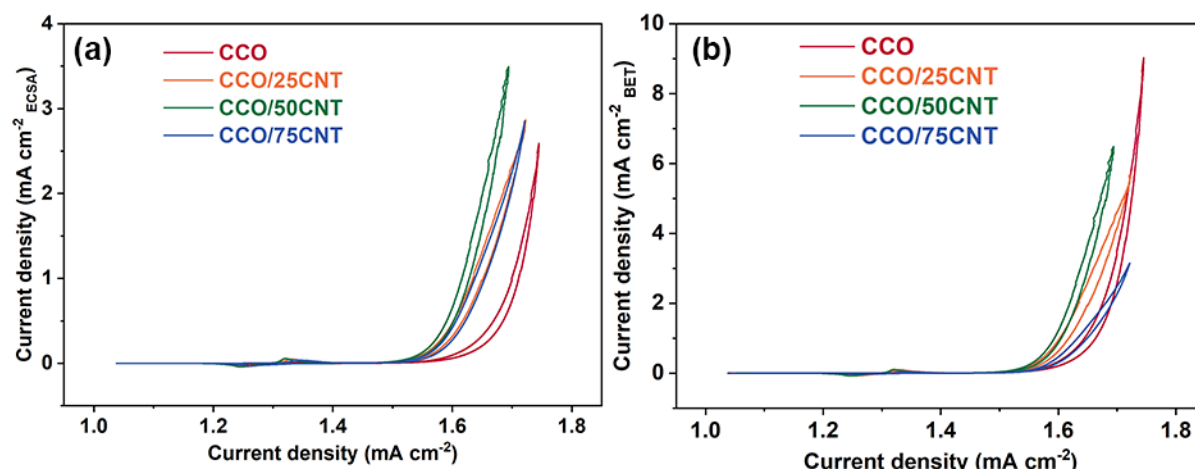**Fig. S13.** N$_2$ adsorption-desorption isotherms (a) and pore structure (b) of CCO and CCO/xCNT (x=25, 50, 75).

Fig. S14. ECSA normalized (a) and BET normalized (b) CV curve of CCO and CCO/xCNT (x=25, 50, 75).
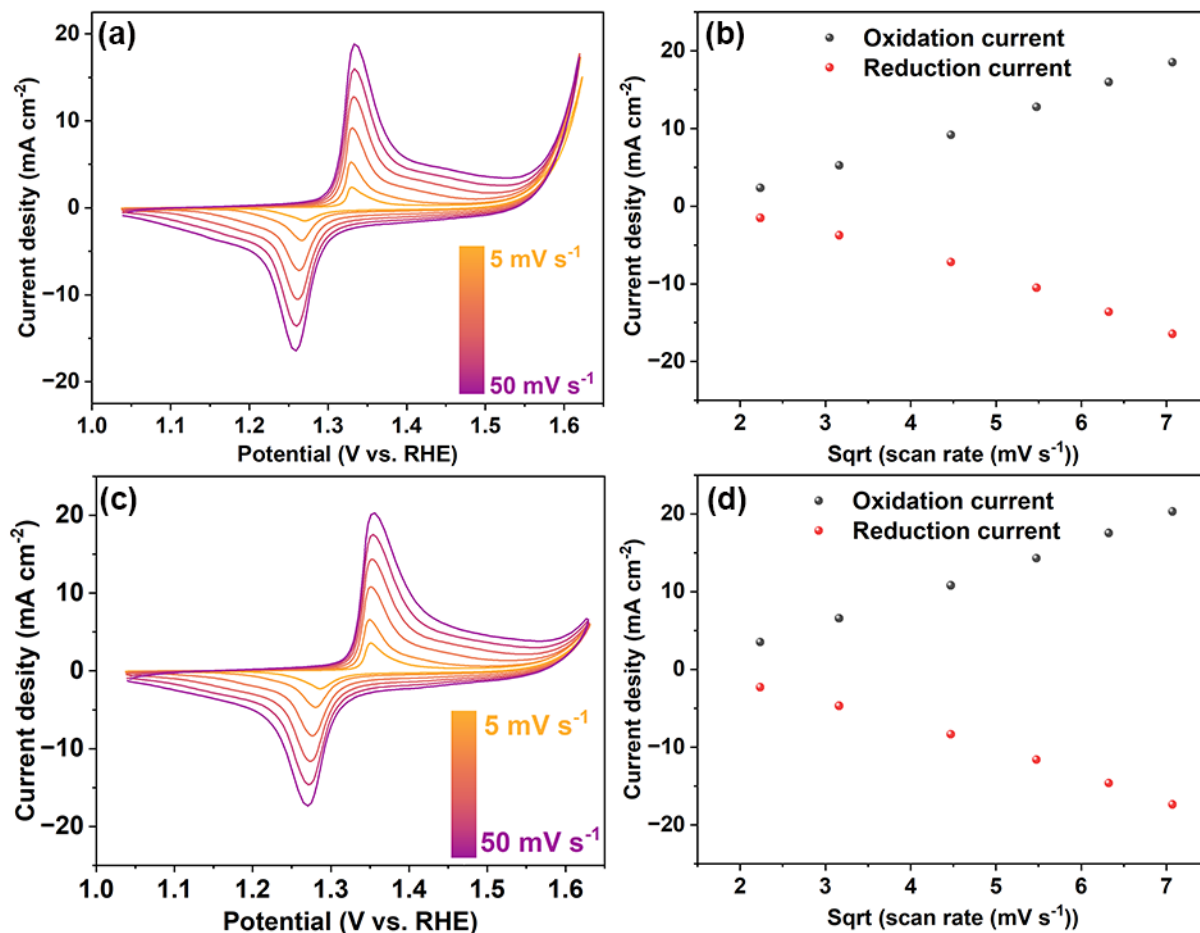
Fig. S15. CVs of Ni@CCO (a) and Ni@CCO/50CNT (c) with different scan rates (5, 10, 20, 30, 40 and 50 mV s^{-1}). The plot of the redox peak currents densities versus the square root of scan rates of Ni@CCO (b) and Ni@CCO/50CNT (d).
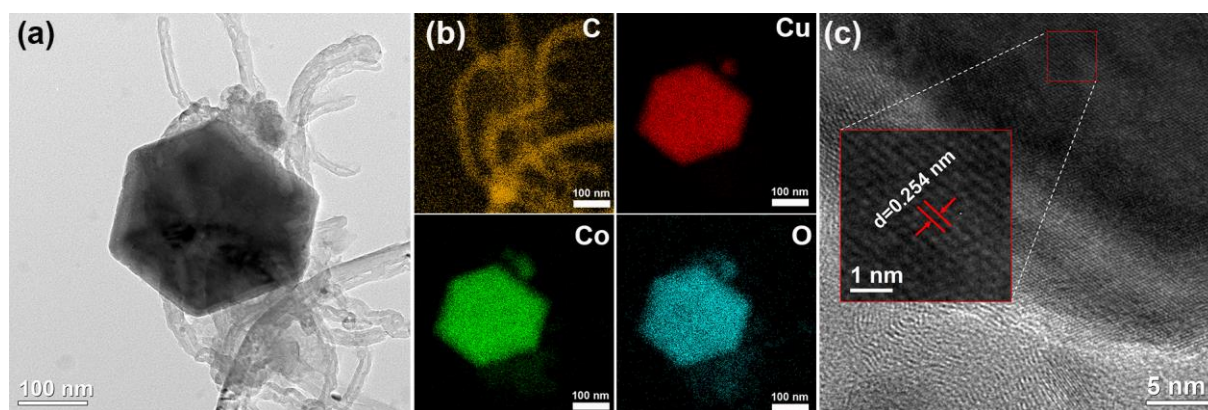
Fig. S16. The TEM images (a), the elemental mappings (b) and the HRTEM images (c) of CCO/50CNT after OER. The inset in (c) is the magnified images.
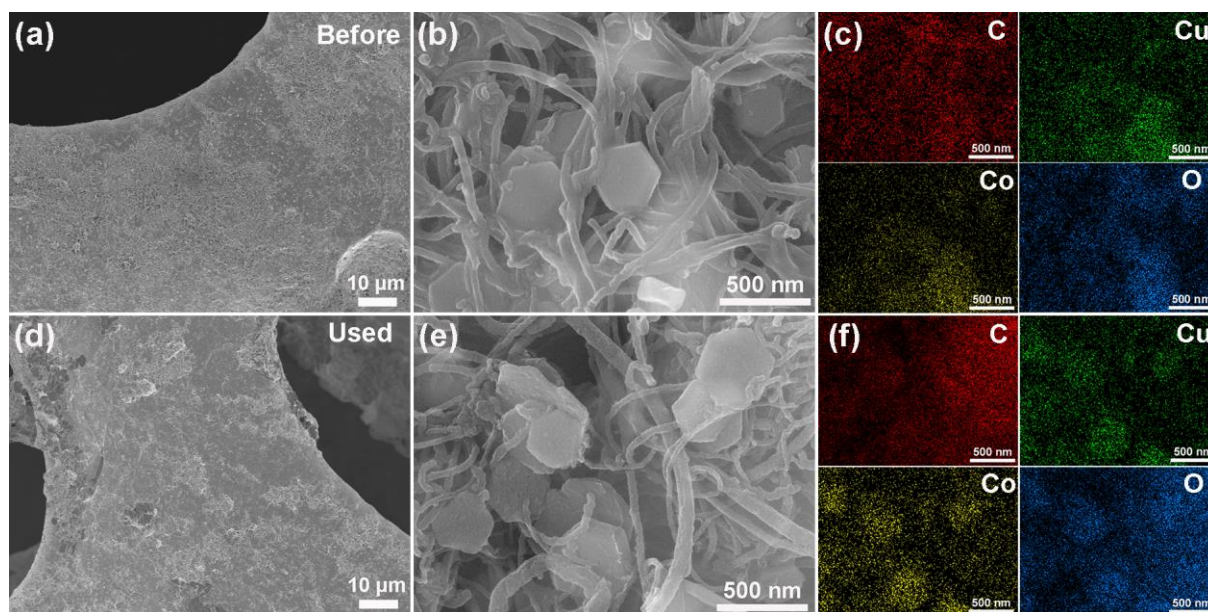
Fig. S17. SEM image (a, b) and elemental maps (c) of Ni@CCO/50CNT before OER. SEM image (d, e) and elemental maps (f) of Ni@CCO/50CNT after OER.
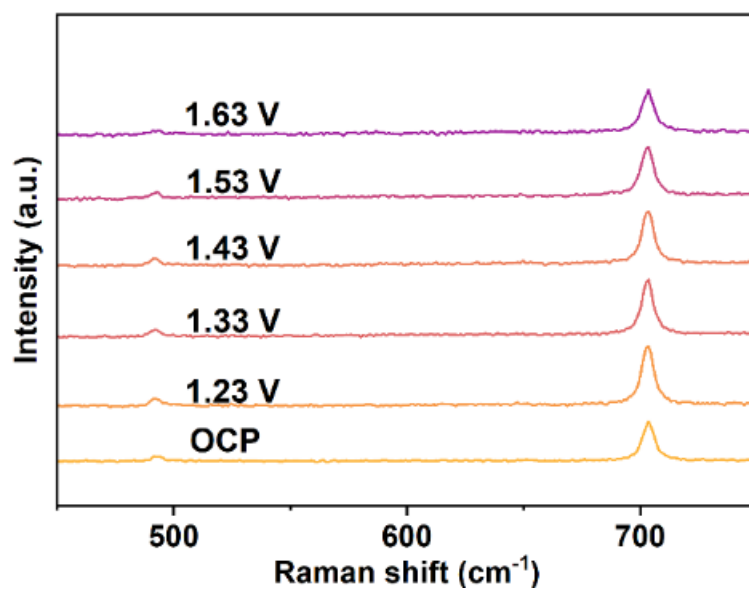
Fig. S18. In situ Raman spectra of Ni@CCO/50CNT in 1.0 M KOH with an open circuit potential (OCP), and applied potential from 1.23 V to 1.63 V (vs. RHE).
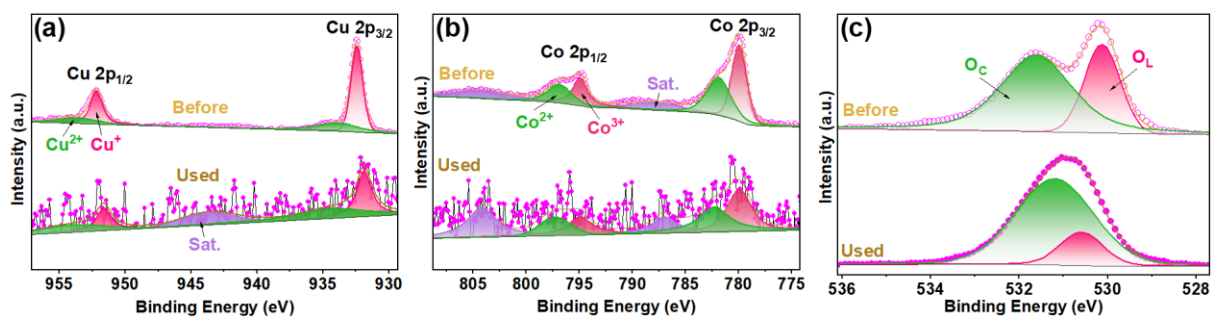
Fig. S19. The high-resolution XPS spectra of Cu 2p (a), Co 2p (b) and O 1s (c) of the Ni@CCO/50CNT before and after OER.
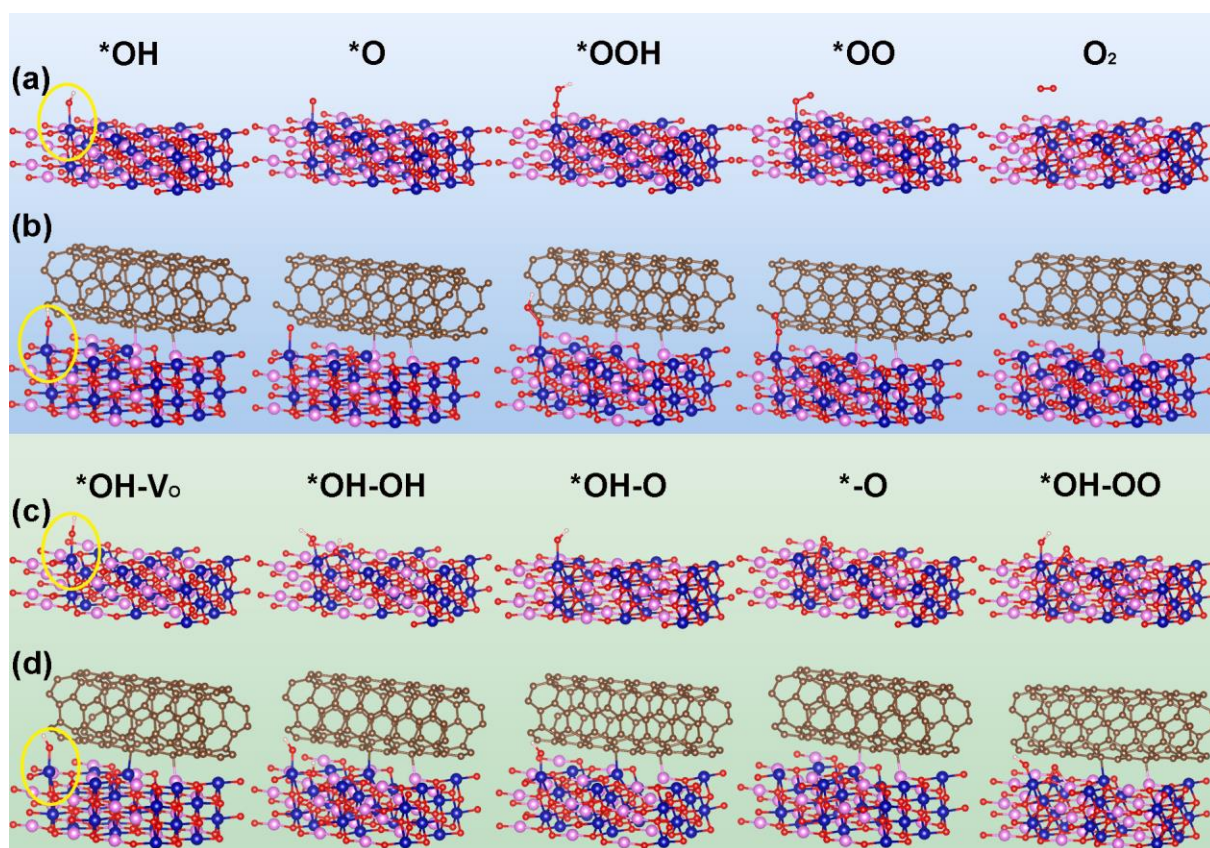
Fig. S20. The slab structures and adsorption intermediates of AEM pathways for CCO (a) and CCO/CNT (b) with V_O. The slab structures and adsorption intermediates of LOM pathways for CCO (a) and CCO/CNT (b) with V_O. The yellow circle is the place where the OER occurs.
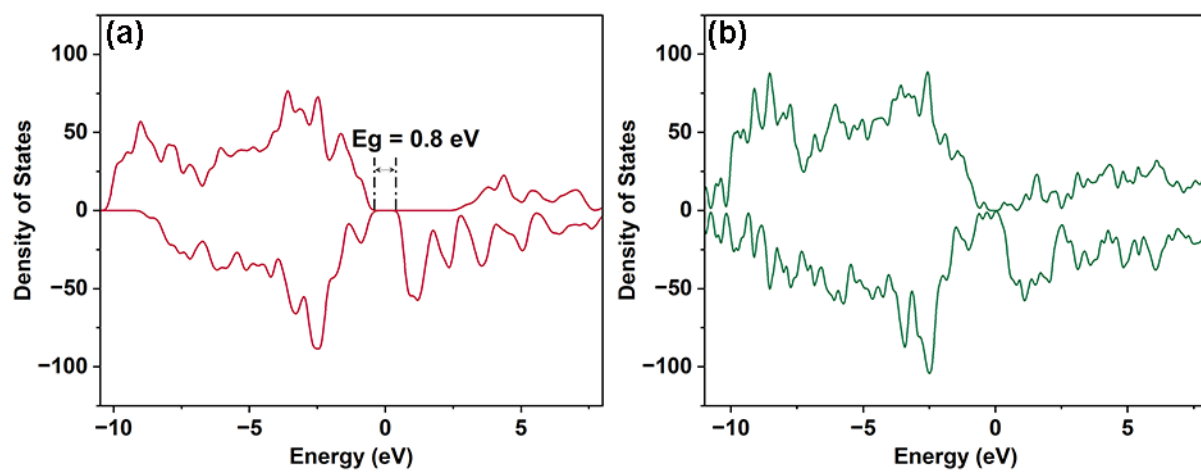
Fig. S21. Total Density of states (TDOS) of CCO (a) and CCO/CNT (b).
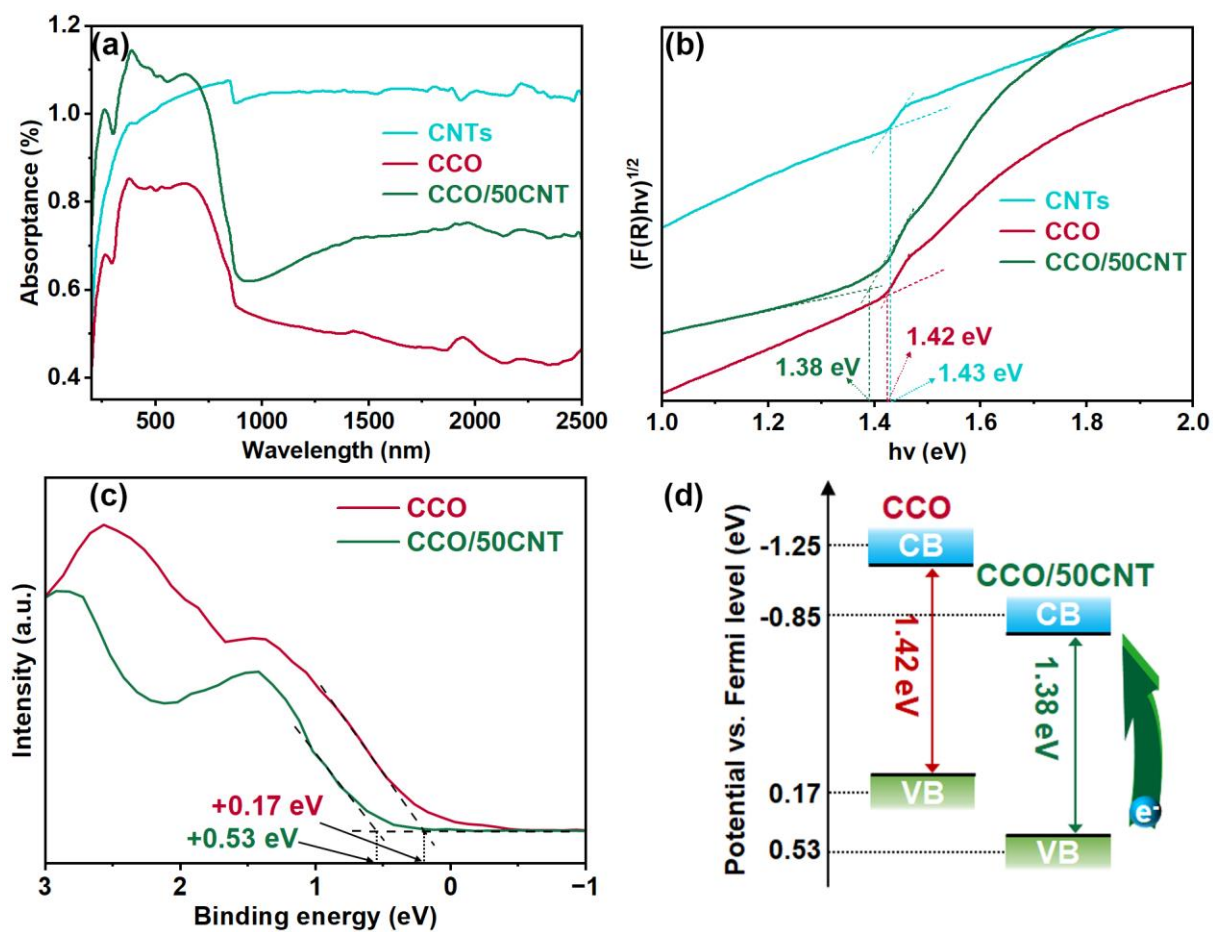
Fig. S22. UV-Vis-NIR absorption spectra and Tauc plots of $[F(R)E]^{1/2}$ for indirect band gap transition of CNTs, CCO and CCO/50CNT; VB XPS spectra (c) and energy band structures (d) of CCO and CCO/50CNT.

Notes and references

1 B. H. Toby and R. B, Von Dreele. General Structure Analysis System (GSAS). *Los Alamos National Laboratory Report LAUR*, 1994: 86-748.

2 B. H. Toby. EXPGUI, a graphical user interface for GSAS. *Journal of applied crystallography*, 2001, **34**(2): 210-213.

3 B. H. Toby and R. B. Von Dreele, GSAS-II: the genesis of a modern open-source all purpose crystallography software package. *J. Appl. Crystallogr.*, 2013, **46**(2): 544-549.

4 G. Kresse and J. Furthmüller, Efficiency of ab-initio total energy calculations for metals and semiconductors using a plane-wave basis set. *Comput. Mater. Sci.*, 1996, **6**(1): 15-50.

5 G. Kresse and J. Furthmüller, Efficient iterative schemes for ab initio total-energy calculations using a plane-wave basis set. *Phys. Rev. B*, 1996, **54**(16): 11169.

6 J. P. Perdew, K. Burke and M. Ernzerhof, Generalized gradient approximation made simple. *Phys. Rev. Lett.*, 1996, **77**(18): 3865.

7 G. Kresse and D. Joubert, From ultrasoft pseudopotentials to the projector augmented-wave method. *Physical review b*, 1999, **59**(3): 1758.

8 P. E. Blöchl, Projector augmented-wave method. *Phys. Rev. B*, 1994, **50**(24): 17953.

9 M. Yang, H. Tan, S. Ma, Y. Mi, L. Liu, Z. Zhao, H. Li and D. Xiong, Gram-scale Solvothermal Synthesis of Fe-doped $CuCoO_2$ Nanosheets and Improvement of Oxygen Evolution Reaction Performance. *Nanoscale*, 2023, **15**(29): 12375-12387.

10 S. Ma, J. Bai, L. Sun, L. Zhao, H. Tan, L. Liu, Z. Peng, X. Zhao and D. Xiong, Investigation of polyethylene glycol (PEG) assisted solvothermal synthesis of $CuCoO_2$ nanosheets for efficient oxygen evolution reaction. *Dalton Trans.*, 2023, **52**(38): 13750-13757.

11 H. Gao, M. Yang, X. Liu, X. Dai, X.-Q. Bao and D. Xiong, Hydrothermal synthesized delafossite $CuGaO_2$ as an electrocatalyst for water oxidation. *Front. Optoelectron.*, 2022, **15**(1): 8.

12 S.-F. Li, B.-Q. Zhang, Y.-N. Li and D. Yan, Regulating the Electronic Structure of Ruddlesden–Popper-Type Perovskite by Chlorine Doping for Enhanced Oxygen Evolution Activity. *Inorg. Chem.*, 2023, **62**(28): 11233-11239.

13 S.-F. Li, J. Zheng, L. Hu, Y. Ma and D. Yan, Facile surface defect engineering on perovskite oxides for enhanced OER performance, *Dalton Trans.*, 2023, **52**, 4207-4213.

14 H. Donya, S. Aman, N. Ahmad, H. M. T. Farid and T. A. M. Taha, Development of $SnCo_2O_4$ spinel supported on the rGO nanosheet with the improved electrochemical performance of OER activity. *Int. J. Hydrog. Energy*, 2024, **51**: 436-447.

15 R. Chen, Z. Wang, S. Chen, W. Wu, Y. Zhu, J. Zhong and N. Cheng, Activating Lattice Oxygen in Spinel Oxides via Engineering Octahedral Sites for Oxygen Evolution. *ACS Energy Lett.*, 2023, **8**(8): 3504-3511.

16 R. Jena, S. Bhattacharyya, N. Bothra, V. Kashyap, S. K. Pati and T. K. Maji, $Ni_xCo_{1-x}@Ni_xCo_{1-x}O$/NCNT as Trifunctional ORR, OER, and HER Electrocatalysts and its Application in a Zn-Air Battery, *ACS Appl. Mater. Interfaces*, 2023, **15**, 27893-27904.

17 R. Jeyagopal, Y. Chen, M. Ramadoss, K. Marimuthu, B. Wang, W. Li and X. Zhang, A three-dimensional porous CoSnS@CNT nanoarchitecture as a highly efficient bifunctional catalyst for boosted OER performance and photocatalytic degradation. *Nanoscale*, 2020, **12**(6): 3879-3887.